# Structural and Mechanistic Insights into Symmetry Conversion in Plant GORK $K^+$ Channel Regulation

Qi-yu Li[1,2#], Li Qin[1,2#], Ling-hui Tang[1,2#], Chun-rui Zhang[1,2#], Shouguang Huang[3], Ke Wang[1,2], Gao-hua Zhang[1,2], Ning-jie Hao[1,2], Qian Xiao[4], Tongxin Niu[4], Min Su[1,2], Rainer Hedrich[3] & Yu-hang Chen[1,2*]

[1]Zero-One Innovation Center and Laboratory of Advanced Breeding Technologies, Institute of Genetics and Developmental Biology, Chinese Academy of Sciences, Beijing 100101, China

[2]University of Chinese Academy of Sciences, Beijing 100049, China.

[3]Molecular Plant Physiology and Biophysics, Julius-von-Sachs-Institute, University of Würzburg, Julius-von-Sachs Platz 2, D-97082, Würzburg, Germany

[4]Center for Biological Imaging, Institute of Biophysics, Chinese Academy of Sciences, Beijing, 100101, China

[#]These authors contributed equally to this work.

[*]Correspondence to:

Yu-hang Chen, E-mail: yuhang.chen@genetics.ac.cn;

**Abstract**

GORK is a shaker-like potassium channel in plants that contains ankyrin (ANK) repeats. In guard cells, activation of GORK causes $K^+$ efflux, reducing turgor pressure and closing stomata. However, how GORK is regulated remains largely elusive. Here, we solved the cryo-EM structure of *Arabidopsis* GORK, revealing an unusual symmetry reduction (from C4 to C2) feature within its tetrameric assembly. This symmetry reduction in GORK channel is driven by ANK dimerization, which disrupts the coupling between transmembrane helices and cytoplasmic domains, thus maintaining GORK in an autoinhibited state. Electrophysiological and structural analyses further confirmed that ANK dimerization inhibits GORK, and its removal restores C4 symmetry, converting GORK to an activatable state. This dynamic switching between C2 and C4 symmetry, mediated by ANK dimerization, presents a GORK target site that guard cells regulate to switch the plant $K^+$ channel between inhibited and activatable states, thus controlling stomatal movement in response to environmental stimuli.

## Main

Potassium ions are essential for plant growth and development, playing roles in osmoregulation, cell expansion, pH homeostasis, and establishing membrane potential and proton motive force[1-2]. In *Arabidopsis thaliana*. 71 potassium channels and transporters have been identified, among which 9 belongs to shaker-like channel family[3]. These channels can be categorized as outward-rectifying types, including GORK and SKOR, or inward-rectifying types, including KAT1, KAT2, AKT1, and AKT2. They sense changes in membrane potential (depolarization or hyperpolarization), regulate potassium transport, and maintain ionic homeostasis, crucial for plant growth and stress response[2,4-7].

GORK, also known as Guard cell Outward-Rectifying $K^+$ channel, is the only outward-rectifying potassium channel in guard cells. Since its discovery in 2000[8], extensive genetic studies have demonstrated its vital role in regulating stomatal movement[9-11]. Stomata, formed by paired guard cells, control water loss and $CO_2$ uptake in response to environmental stimuli, thereby regulating transpiration and photosynthesis[8,12-17]. Ion channels in guard cells control turgor pressure by mediating ion flux, which in turn regulates stomatal opening and closing[2,5,18]. KAT1 presents the major guard cell potassium uptake channel, required for increasing turgor pressure and volume increase promoting stomatal opening. In contrast GORK activation causes potassium efflux, reducing guard cell turgor and volume and in turn stomatal closure[3,8-9,12,19].

Understanding the structure and function of these channels is critical for unraveling their roles in ion homeostasis and stomatal movement. So far, the structural study of plant KAT1 have provided important insights into its activation and role in potassium influx control[20-21]. However, the structure and regulatory mechanisms of GORK remain largely enigmatic. Unlike the inward-rectifying KAT1, the outward-rectifying GORK harbors a unique ankyrin (ANK) repeat domain, whose functional role in plant ion channel regulation remained yet unexplored.

65 In this study, we report the cryo-EM structures of *Arabidopsis* GORK (*At*GORK)
66 in both autoinhibited state and activatable state. The full-length *At*GORK$^{FL}$ forms a
67 tetramer with elongated cytoplasmic regulatory domains, with its architecture showing
68 a symmetry reduction from four-fold (C4) to two-fold (C2). Remarkable, ANK from
69 neighboring protomers interact to form dimers, thus reducing symmetry of the tetramer
70 and rendering GORK in an autoinhibited state. Electrophysiological studies show that
71 mutations or truncations disrupting ANK interactions convert GORK into an
72 activatable state. Further structural analysis of ANK-truncated *At*GORK$^{623}$ and
73 *At*GORK$^{510}$ reveals that the cytoplasmic regulatory domains become highly dynamic,
74 while strict C4 symmetry is restored in the tetrameric assembly.
75 Thus, our study demonstrates that ANK acts as a molecular switch for symmetry
76 conversion (between C2 and C4), regulating GORK conformational transitions between
77 autoinhibited and activatable states. This research provides the first comprehensive
78 elucidation of the biological role of ANK in GORK, offering new insights into how
79 GORK mediates stomatal closure in response to environmental signals. Furthermore,
80 our findings broaden the understanding of ion channel regulation, particularly how
81 symmetry changes in structural assembly regulate ion channel activity.
82
83
84 **Cryo-EM structure determination of the *Arabidopsis* GORK**
85 To elucidate the structure of the GORK, we prepared *Arabidopsis* GORK (fused with
86 an N-terminal GFP tag) from HEK293 cells and conducted single particle cryo-EM
87 analysis. After solubilization in 1.0% n-Dodecyl-B-D-Maltoside (DDM) and 0.02%
88 cholesteryl hemisuccinate (CHS), the *At*GORK proteins underwent purification
89 through strep-tactin affinity chromatography, GFP removal via TEV enzyme cleavage,
90 and subsequent gel-filtration chromatography. The final solution contained 0.006%
91 detergent GDN, 150 mM NaCl, and 20 mM HEPES-Na pH 6.5. The most monodisperse
92 peak fractions were pooled and concentrated to approximately 3.5 mg/mL for cryo-EM
93 grid preparation.

We determined the cryo-EM structures of the full-length *At*GORK (*At*GORK$^{FL}$, residues 1 to 820) in an auto-inhibited state, along with two ANK-truncated versions (*At*GORK$^{623}$, residues 1 to 623; *At*GORK$^{510}$, residues 1 to 510) (Table S1, Supporting Information). Tetrameric reconstructions of *At*GORK were obtained in two conformational states at resolutions of 3.4 Å (*At*GORK$^{FL1}$) and 4.3 Å (*At*GORK$^{FL2}$), allowing *de novo* modeling of 662 of 820 amino acids (residues 58 to 720) for each protomer, while the remaining regions were not resolved due to their intrinsic flexibility (Figure S1, Supporting Information). For the truncated *At*GORK$^{510}$ and *At*GORK$^{623}$, cryo-EM maps at 3.4 Å and 3.2 Å resolution, respectively, were obtained. Both maps showed high-quality density in their transmembrane domain, allowing accurate modeling, while the flexible cytosolic domains remained unmodeled due to their invisibility (Figure S2, Supporting Information). Structure-based sequence alignment for 24 representative GORKs from both monocots and dicots is shown in Figure S3, Supporting Information.

**Architecture of *Arabidopsis* GORK in symmetry-reduced conformation**

*Arabidopsis* GORK (*At*GORK) forms a homo-tetrameric structure around a central pore, with a dimension of 110 Å (length) × 110 Å (width) × 170 Å (height) (Figure 1A-C). Each protomer has an N-terminal transmembrane domain (TMD, residues 58-313, containing helices S1-S6), followed by three cytoplasmic domains: the C-linker (residues 314-365), CNBDH (residues 366-510), and ANK (residues 511-724). The segment preceding the TMD (residues 1-57) and the last portion (residues 725-824, containing a putative KHA domain enriched in hydrophobic and acidic residues) are not visible in the structure, likely due to their intrinsic flexibility or the flexibility of the connecting regions.

The *At*GORK structure, unlike other tetrameric ion channels such as KAT1, exhibits a unique architectural assembly[20]. Notably, the symmetry in the TMD portion adopts a typical four-fold (C4), but reduces to a two-fold (C2) in their following

122 cytoplasmic domains, thus leading to a deformation within the tetrameric channel
123 (Figure 1D). Superimposition of its protomer reveals distinct conformations, with
124 notable rotations and displacements occurred in the C-linker, CNBDH, and ANK
125 domains (Figure 1E). This symmetry reduction within the tetrameric assembly appears
126 to arise from ANK dimerization (will discuss later). To the best of our knowledge, this
127 symmetry reduction in channel assembly is exceptionally rare and leads to deformation
128 of the tetrameric channel. This represents a unique structural feature of the GORK
129 family and likely serves as a unique mechanism for channel regulation. Thus, the
130 current *At*GORK structure likely represents an autoinhibited, pre-activation state.

131 The TMD consists of a voltage sensing domain (VSD, helices S1–S4) and a pore-
132 forming domain (PD, helices S5 and S6) (Figure 2A). The VSD is connected to the PD
133 through a short linker, resulting in a "non-domain-swapped" configuration where the
134 VSD and PD of the same subunit form a cohesive bundle. This differs from the
135 canonical domain-swapped architecture in Shaker-like[22] and $Na_V$ channels[23], where
136 the VSD and PD are separated by a long S4−S5 linker. The P-loop segment of *At*GORK
137 contains a highly conserved motif ($^{271}$TVGYG$^{275}$), similar to that of bacterial KcsA[24],
138 mammalian HCN[25], and plant outward-rectifying SKOR[26] and inward-rectifying
139 KAT1[20] and AKT1[27]. Structural comparisons reveal that they form a similar $K^+$
140 selectivity filter (Figure S4A, Supporting Information). Analysis using the HOLE[28]
141 suggests that the *At*GORK adopts a closed conformation. Below the selectivity filter
142 lies the pore gate region consists of residues on the S6 helix, with I303 and T307
143 creating narrowest constrictions (radius of approximately 1 Å). The S4 helix contains
144 conserved positively charged residues (R174, R177, R179, and R187), and adopt a
145 resting "up" conformation, similar to that in plant inward-rectifying KAT1[20] and
146 AKT1[27] (Figure S4B, Supporting Information).

147 After the TMD, the C-linker is positioned next to the helix bundle crossing,
148 connecting the transmembrane helices to the cytoplasmic domains. It comprises four
149 helices (A'-D'), forming two "helix-turn-helix" motifs. These helices further assemble

into a gating ring architecture within the tetrameric channel through "elbow-on-shoulder" inter-subunit interactions, where helix A'-turn-helix B' (elbow) of one protomer interacts with helix C'-turn-helix D' (shoulder) of its neighboring protomer[29] (Figure 1C). Due to the reduced symmetry within the tetramer, the C-linkers exhibits distinct conformations between adjacent protomers, either "flat" or "kinked" (Figure 2B). Consequently, the C-linker in *At*GORK deviates from C4 symmetry, and the presence of the "flat" conformation disrupts the formation of a C4 symmetrical gating ring, leading to decoupling between the transmembrane helices and the cytoplasmic domains, ultimately affecting channel gating.

The CNBDH domain, connected to the C-linker, shares approximately 20% sequence identity with canonical cyclic nucleotide-binding domains (CNBDs) (Figure S5A, Supporting Information), which play crucial roles in regulating channels, kinases and transcription factors upon binding to secondary messengers (cAMP or cGMP). Despite low sequence homology, the CNBDH share a similar structural fold to those of the CNBDs (Figure S5B, Supporting Information). The CNBDH of GORK consists of four short α-helices (A, P, B, and C) and an eight-stranded β-roll (β1- β8) (Figure 2C). Helix A is located before the β-roll, Helix P is inserted within the β-roll (between β6 and β7), and Helices B and C are positioned afterward. Helices A and B interact in an antiparallel manner, and the putative phosphate-binding cassette comprises β6, Helix P, and β7.

Although the CNBDH shares overall structural similarity with animal CNBDs, there are notable differences (Figure S5B, Supporting Information). GORK lacks conserved residues for cAMP binding, such as R561 in 7lfx or R620 in 2ptm, which is replaced by Q465. More strikingly, alanine at the binding pocket entrance (A563 in 7lfx[30], or A622 in 2ptm[29]) is replaced by bulky phenylalanine (F467 in *At*GORK), likely blocking nucleotide access. Helix C also adopts a closed conformation, with its adjacent loop obstructing the binding site entrance, suggesting that large conformational changes would be required for cyclic nucleotide binding.

178 Following the CNBDH, six ankyrin repeats fold into a single ANK domain,
179 forming a slightly curved solenoid structure (Figure 2D). The first three repeats
180 (ANK1-3) and the last three repeats (ANK4-6) are tandem units with ~34% sequence
181 identity. In each tandem unit, two repeats are canonical, consisting of a pair of anti-
182 parallel α-helices and an intervening "finger" loop, while the third is a degenerate repeat
183 lacking the "finger" loop. Remarkably, ANK repeats from two neighboring protomers
184 forms a stable dimer through specific interactions mediated by their protruding loops,
185 creating a buried area of ~1500 $Å^2$. This dimeric interaction is specific, corroborated
186 by another structure of the full-length of *At*GORK$^{FL2}$, which retains similar dimeric
187 units despite of variation in their tetrameric conformations (Figure S1E, Supporting
188 Information). A similar ANK dimerization pattern has also been observed in SKOR
189 (Figure S1F, Supporting Information)[26], suggesting that this dimerization is a common
190 structural feature in outward rectifying plant ANK-containing $K^+$ channels.
191 As a result of ANK dimerization, positional deviations and conformational
192 changes are induced in the adjacent CNBDH and C-linker, leading to a reduction in
193 symmetry within the tetrameric channel. This reduction affects the communication and
194 coupling between cytoplasmic domains and transmembrane helices, ultimately
195 maintaining GORK in an autoinhibited, pre-activation state. The structures of GORK
196 and SKOR with reduced symmetry provide crucial insights into how the ANK domain
197 regulates these channels, maintaining them in an autoinhibited conformation under
198 resting conditions. This is supported by the observation of basal activity of full-length
199 *At*GORK.
200
201 **ANK dimerization maintains GORK channel in an auto-inhibited state**
202 The ANK repeats and their dimeric interactions are distinctive features of the GORK
203 channel, playing a key role in reducing symmetry within its tetrameric assembly. To
204 explore their function, we conducted trunctional analysis of the ankyrin repeats in
205 *At*GORK expressed in *Xenopus oocytes* and inspected via TEVC electrophysiology

206 (Figure 3A). Full-length *At*GORK produced basal currents, indicating that a small
207 fraction of these channels was in an activatable state. Removing the KHA domain while
208 retaining the intact ANK domain in *At*GORK (Δ737-820, residues 1-736) led to a slight
209 increase in oocytes currents, whereas deleting the last three C-terminal ANK repeats
210 (Δ624-820, residues 1-623) significantly enhanced current amplitude—reaching 13.3-
211 fold that of the full-length channel at +70 mV (Figure 3B, C). However, removing all
212 six ANK repeats produced more complex outcomes depending on the truncation site:
213 Δ544-820 (residues 1-543) further increased current amplitude to approximately 26.3-
214 fold that of the wild-type full-length channel, while Δ528-820 (residues 1-527)
215 decreased current amplitude, and Δ511-820 (residues 1-510) nearly abolished the
216 currents (Figure 3B, C).

217 To rule out the possibility that these changes in current were due to trafficking
218 defects, we fused a GFP tag to the N terminus of these ANK truncation mutants and
219 observed that their surface expression levels were comparable to that of the wild-type
220 channel (Figure S6A, B, Supporting Information). Therefore, the enhanced currents in
221 the truncation mutants are primarily due to the disruption of ANK dimerization, which
222 in turn releases *At*GORK from its autoinhibited state. These findings indicate that ANK
223 dimerization is responsible for maintaining the autoinhibited state of *At*GORK, and the
224 channel becomes activatable upon autoinhibition release. Moreover, the helix from the
225 first ANK repeat (residues 520–543), which is directly connected to the CNBDH, is
226 essential for the transition of *At*GORK from the autoinhibited to the activated state.

227 The dimerization of ANK is driven by hydrophobic interactions mediated by the
228 hairpin loops protruding from the ankyrin repeats. Inspired by this structural insight,
229 we replaced the hairpin loop with an unrelated short "SGGG" motif. Notably,
230 substituting the loops between repeats 1/2 and 2/3 significantly enhanced *At*GORK
231 activity, whereas similar replacement between repeats 4/5 and 5/6 impaired *At*GORK
232 function (Figure 3D, E). To rule out the possibility that these mutations affected channel
233 trafficking, we also performed GFP fusion analysis on the resutant mutants (Figure S6A,

234 B, Supporting Information), which confirmed normal surface expression levels. This
235 aligns well with findings from ANK truncational studies (Figure 3B, C), confirming
236 that disrupting ANK dimeric interactions release *At*GORK from autoinhibition and thus
237 allowing channel activation. However, these observations also suggest that the ANK
238 repeats in GORK have a more complex role than initially anticipated: they are not only
239 essential for maintaining the autoinhibited state but also play a pivotal role in stabilizing
240 the open state during channel activation.
241
242 **Mutational test on conserved acidic residues at the C-linker/TMD interface**
243 The C-linkers assemble into a disc-shaped gating ring via "elbow-on-shoulder"
244 interactions[29], directly contacting the TMD and playing a crucial role in channel gating.
245 Conserved negatively charged residues, including E317, D321, and D325, are
246 positioned on the C-linker A' helix, forming a negatively charged ring at the entrance
247 of the ion-conducting pathway (Figure 4A) and engaging in an intricate interaction
248 nexus with conserved K/R from the TMD (Figure 4B). Specifically, E317 and D321
249 (C-linker of protomer A) form ionic interactions with K312 (Helix S6' of protomer D),
250 while R200 (Helix S5 of protomer A) forms a salt bridge with E317 from its adjacent
251 protomer B. In such a fashion, the C-linker-mediated gating ring is connected with the
252 VSD and PD within the TMD through their domain-swapped interfaces. These three
253 residues correspond to conserved R, D, and A in the inward $K^+$ channels KAT1[20] and
254 AKT1[27], respectively.
255 To further validate their functional role, we introduced the mutations, E317R,
256 D321 (N or R), and D325A into both full-length *At*GORK and the ANK-truncated
257 *At*GORK$^{543}$ construct. In full-length GORK, E317R and D325A enhanced current
258 amplitude, whereas D321N and D321R produced an even larger increase (Figure S7A,
259 B, Supporting Information). In contrast, in the activatable ANK-truncated *At*GORK$^{543}$,
260 E317R and D325A partially reduced the current amplitude, yet it remained higher than
261 that of the wild-type full-length *At*GORK, while D321N and D321R still significantly

262 enhanced the currents (Figure 4C, D). In addition, these mutants exhibited distinct
263 alterations of half-activation voltage ($V_{1/2}$) in their $G_{relative}$–$V$ relationships: $V_{1/2}$ of
264 E317R negatively shifted in full-length *At*GORK but showed slightly positively shifted
265 in *At*GORK$^{543}$; $V_{1/2}$ of D325A had no apparent shift in the full-length construct but
266 positively shifted in GORK$^{543}$; and $V_{1/2}$ of D321N and D321R negatively shifted in
267 both constructs (Figure 4E, F; Figure S7C, D, Supporting Information).
268 Intriguingly, E317R and both D321 mutations (D321N and D321R) exhibited
269 significant changes in deactivation kinetics. Specifically, when the membrane potential
270 was held at -110 mV following the test voltage, the tail current decay was markedly
271 delayed (Figure 4C; Figure S7A, Supporting Information). For D321N, the deactivation
272 time constant ($t_{1/2}$) was prolonged in both the full-length GORK and the ANK-truncated
273 *At*GORK$^{543}$, increasing from 75 ms to 1992 ms, and from 34 ms to 1687 ms,
274 respectively (Figure 4G; Figure S7E, Supporting Information). Moreover, D321N
275 accelerated the activation kinetics, with $t_{1/2}$ decreasing from 462 ms to 286 ms in the
276 full-length, and from 261 ms to 147 ms in the truncated form respectively (Figure 4G;
277 Figure S7E, Supporting Information). Notably, inward $K^+$ tail currents were observed
278 during the -110 mV holding phase, indicating that these mutations disrupted the original
279 outward rectification, thereby allowing inward $K^+$ flow.
280
281 **Disrupting ANK-dimerization relieves constraints and restores C4 symmetry**
282 Our structural studies reveal that ANK dimerization in full-length *At*GORK is directly
283 responsible for reducing its tetrameric symmetry from C4 to C2, maintaining an
284 autoinhibited state. Under resting conditions, GORK shows minimal basal currents,
285 whereas ANK-truncated mutants, including *At*GORK$^{623}$ and *At*GORK$^{543}$, show
286 significantly increased currents, suggesting that ANK truncations relieve autoinhibition
287 and enhances GORK activity. Structural analysis of *At*GORK$^{623}$ and *At*GORK$^{510}$ only
288 resolved the TMD portion, with their cytoplasmic regions being too flexible for
289 visualization (Figure S2, Supporting Information). These findings suggest that ANK

290 truncation relieves the autoinhibitory constraints imposed by ANK dimerization,
291 converting *At*GORK into an activatable state.

292 Structural analysis also provided some clues regarding the restoration of C4
293 symmetry in the *At*GORK. Firstly, the structures of *At*GORK$^{623}$ and *At*GORK$^{510}$ are
294 highly similar, with a root-mean-square deviation (RMSD) of approximately 0.48 Å for
295 their superimposed tetramers (Figure 5A). Importantly, the ANK-truncated protomers
296 exhibit strict C4 symmetry, with RMSDs of approximately 0.16 Å/256 superimposed
297 Cα. In contrast, the TMD of full-length *At*GORK$^{FL1}$ displays quasi-C4 symmetry
298 (essentially C2 symmetry), with subtle yet distinct differences between protomers A/C
299 and B/D at the N-terminal end of helix S5, yielding an RMSD of approximately 0.75
300 Å/256 superimposed Cα (Figure 5B, C). A comparison of protomers A and B in both
301 *At*GORK$^{FL1}$ and *At*GORK$^{623}$ reveals that the protomers in *At*GORK$^{623}$ closely
302 resembles protomer A in *At*GORK$^{FL1}$, rather than protomer B (Figure 5D). This
303 suggests that ANK dimerization results in C2 symmetry in the full-length *At*GORK$^{FL1}$,
304 whereas ANK truncation restores C4 symmetry in the *At*GORK$^{623}$.

305 We also performed AlphaFold3-based modeling on *At*GORK$^{623}$, showing that the
306 TMD of the predicted *At*GORK$^{623}$ structure is highly similar to that obtained by cryo-
307 EM, with an RMSD of 1.97 Å for the superimposed tetramers. However, the subsequent
308 portions, including the C-linker, CNBD, and ANK domains, are in a loose and relaxed
309 conformation. Due to the lack of ANK dimerization, the overall structure exhibits C4
310 symmetry (Figure S8, Supporting Information). Together with our structural and
311 electrophysiological data, these observations support the role of ANK as a molecular
312 switch for symmetry conversion in GORK, revealing a novel mechanism for channel
313 regulation via symmetry conversions.

314

315 **A model for symmetry conversion in GORK regulation**

316 In summary, our analysis shows that full-length *At*GORK$^{FL}$ adopts C2 symmetry due
317 to ANK dimerization in the cytoplasm. Cryo-EM and AlphaFold3 modeling of ANK-

318 truncated *At*GORK$^{623}$ reveal a restoration of C4 symmetry within the tetrameric
319 assembly. This symmetry conversion, driven by ANK dimerization, regulates
320 intermodular communication and channel gating process. The transition between C2
321 and C4 symmetry governs GORK switching between autoinhibited and activatable
322 states. In short, ANK dimerization maintains GORK in C2 symmetry and an
323 autoinhibited state, while disrupting ANK dimerization restores C4 symmetry and
324 activates GORK (Figure 6). Thus, the ANK domain acts as a molecular switch for
325 symmetry conversion, providing a finely tuned mechanism for GORK regulation.
326

327 **Discussion**

328 Plant potassium channels are crucial for $K^+$ transport and maintaining potassium
329 homeostasis[2]. In *Arabidopsis*, nine Shaker-like potassium channels contain multiple
330 modular domains in their architectures, including the pore-forming TMD, the
331 regulatory C-linker, and CNBD, with some also containing ANK and KHA domains.
332 Based on the presence of the ANK domain, these channels can be divided into two
333 groups: ANK-free members (KAT1, KAT2, and KC1) and ANK-containing members
334 (GORK, SKOR, AKT1, AKT2, AKT5, and AKT6). Currently, structural information
335 are available for KAT1[20-21], SKOR[26], and AKT1[27,31], allowing us to conduct
336 systematic comparative analysis

337 In ANK-free KAT1, structural studies show that it forms a symmetric tetramer
338 with typical C4 symmetry throughout both the transmembrane and intracellular
339 regions[20-21], similar to animal cyclic nucleotide-gated channels (CNGC)[30]. In contrast,
340 GORK, which contains a unique ANK domain, exhibits a symmetry transition from C4
341 in the transmembrane region to C2 in the cytoplasmic region, resulting in distinct
342 structural features. A similar symmetry reduction is observed in other ANK-containing
343 potassium channels, such as AKT1[27] and SKOR[26]. This reduction in symmetry is rare
344 among ion channels, suggesting it may be a unique feature of ANK-containing channels
345 linked to their regulatory mechanisms.

346 Our study provides the first clear-cut evidence that ANK acts as a molecular switch
347 controlling GORK channel symmetry and activity. Structural analysis reveals that ANK
348 dimerization holds GORK in an autoinhibited state at rest. ANK dimerization mediates
349 interactions between protomers, reduces tetramer symmetry, and causes the
350 displacement of internal, highly mobile modules, with neighboring CNBDH and C-
351 linker shifting from C4 symmetry to C2. The C-linker adopts two different
352 conformations: "kinked" and "flat" (Figure 2B). The "kinked" conformation is common
353 in C4 symmetric channels, while the "flat" conformation is unique to ANK-containing
354 channels with reduced symmetry. Subtle yet distinct differences in the S5 helices
355 between adjacent protomers in *At*GORK$^{FL1}$ renders a quasi-C4 symmetry in the TMD
356 (Figure 5B). The reduction in GORK symmetry signifies an autoinhibited state,
357 supported by the observed basal electrophysiological activity.
358 Our ANK truncation experiments showed that ANK removal converts GORK
359 from an autoinhibited to an activatable state, as evidenced by enhanced activities in the
360 truncated *At*GORK$^{543}$ and *At*GORK$^{623}$ variants upon membrane depolarization (Figure
361 3B-E). Structural analysis further revealed that the TMD restores strict C4 symmetry,
362 while the C-linker and CNBDH become highly mobile in these ANK-truncated mutants.
363 Additionally, AlphaFold3-based modeling confirmed that disrupting ANK
364 dimerization relieves constraints and restores C4 symmetry in the tetramer, enabling
365 GORK transition to an activatable state. Thus, ANK serves as a molecular switch to
366 regulate GORK activity by controlling the symmetry conversion of its tetrameric
367 assembly.
368 Ankyrin domains also occur in TRPV channels, where they form a “petal-like”
369 arrangement in the cytoplasm and act independently rather than directly participating
370 in channel assembly[32]. Typically, these domains consist of six ankyrin repeats,
371 forming a “palm-and-finger” structure, whose concave surface binds cytoplasmic
372 proteins or ligands. Unlike GORK, and TRPV gating depends on ANK conformational
373 changes, such as rigid-body rotation. In TRPV4, RhoA binding to the ANK domain

374 inhibits channel activity, whereas calmodulin binding enhances it, highlighting the
375 versatile roles of ANKs in fine-tuning channel activity and coordinating intracellular
376 signaling.

377 The autoinhibited-to-activatable transition of the GORK channel is governed by
378 the dimerization state of its ANK domain, yet the molecular triggers of this dimerization
379 and its reversal remain unknown. A recent study suggests that the cytosolic N-terminus
380 of GORK functions as a "safety catch", constraining its transitions toward the open
381 state[33]. In the truncated mutant GORK$^{\Delta 23}$, removal of the N-terminal segment not only
382 relieves autoinhibition and markedly enhances channel activity, but also restores C4
383 symmetry in the pre-opened conformation. This provides additional evidence for a C2–
384 C4 symmetry switch during channel assembly. Thus, both the N- and C-termini are
385 crucial for GORK regulation, but how they cooperate is still to be elucidated.

386 Previous studies showed that phosphorylation affects ANK-mediated protein-
387 protein interactions and channel activity[32,34-35]. Several protein kinases, including
388 CPK21[36] and CPK33[37], have been identified as candidates for regulating GORK
389 activity, with phosphorylation sites, such as S649 in the ANK domain[38]. However, the
390 molecular mechanisms of these kinases require further investigation. A parallel case is
391 AKT1, which is activated by CIPK23 and CBL1, with multiple potential
392 phosphorylation sites identified (including within its ANK domain). The low-resolution
393 structure of AKT1 co-expressed with CIPK23 and CBL1 shows C4 symmetry in the
394 CNBDs, though it remains unclear whether this is due to ANK phosphorylation[27].

395 Autoinhibition is an intrinsic mechanism that maintains ion channels and
396 transporters in an inactive state, conserving energy in the resting state. In plants,
397 different proteins achieve this through distinct molecular strategies. For example,
398 SLAC1—a guard-cell anion channel essential for stomatal closure—is held in its
399 autoinhibited state by interactions between its N-terminal domain and the pore-forming
400 transmembrane region; phosphorylation relieves this inhibition, rendering the channel
401 activatable[39]. By contrast, GORK utilizes its ANK domain as a molecular switch:

402 ANK dimerization reduces the tetramer symmetry (from C4 to C2) to ensure
403 autoinhibition, while disrupting ANK dimerization restores C4 symmetry and allows
404 GORK becoming activatable. Together, these cases highlight the diversity of
405 auto-inhibition mechanisms and shed light on their roles in plant physiology.

406 In summary, our study reveals that ANK regulates GORK channel activity through
407 tetrameric symmetry conversion. Under resting conditions, ANK dimerization
408 maintains GORK in a C2 symmetric conformation, maintaining it in a preactivated,
409 autoinhibited state. In response to environmental stimuli, GORK undergoes a symmetry
410 conversion and runs into an activatable state, enabling $K^+$ efflux and stomatal closure.
411 This mechanism provides new molecular insights into stomatal regulation and offers
412 potential avenues for developing improved crop varieties through ANK engineering.
413

414 **Methods**

415 **Expression and purification of the GORK proteins**

416 The genes of *Arabidopsis* full-length *At*GORK (AT5G37500) and truncated variants
417 (*At*GORK$^{623}$, residues 1-623 and *At*GORK$^{510}$, residues 1-510) were cloned into a
418 modified pEG BacMam vector, which included a PreScission protease cleavage site,
419 GFP, an 8× His tag, twin-Strep tag, and Flag tag at the N-terminus. Recombinant
420 proteins were expressed in HEK293F cells. In short, baculovirus was generated in *Sf9*
421 insect cells, and P2 viruses were used to infect HEK293F cells. Cells were cultured in
422 suspension, supplemented with 1% (v/v) fetal bovine serum, and maintained at 37 °C
423 with 70% humidity and 6% $CO_2$. Cells were infected with P2 viruses at a density of
424 approximately $2.6\times10^6$ cells/mL, and supplemented with 10 mM sodium butyrate upon
425 8 hours post-infection, and continued to grow at 30°C for another 50 hours. Cells were
426 harvested, centrifuged, and stored at -80°C.

427 Harvested cells from a 300 mL of culture were resuspended in extraction buffer
428 (20 mM HEPES-Na pH 8.0, 150 mM KCl, 10 mM DDM, 2 mM cholesteryl
429 hemisuccinate (CHS) supplemented with protease inhibitors (2 μg/mL pepstatin, 2
430 μg/mL aprotinin, 2 μg/mL leupeptin and 1mM phenylmethylsulfonyl fluoride) and
431 incubated at 4°C for 2 hours. Solubilized membranes were clarified by centrifugation
432 at 41,000 rpm for 1 hour, and the supernatant was loaded onto a Streptactin Beads 4FF
433 column. Following a 5-column volume buffer wash, proteins were eluted with
434 solubilization buffer (20 mM HEPES-Na pH 8.0, 150 mM KCl, 0.02% GDN, and 2.5
435 mM desthiobiotin). After tag removal with TEV protease, the proteins were further
436 purified using a Superose-6 column in solubilization buffer (20 mM HEPES-Na pH 8.0,
437 150 mM KCl, 0.006% GDN). The elution was analyzed by SDS-PAGE, and the peak
438 fractions of the purified protein were pooled and concentrated to ~3.5 mg/mL.

439 For the preparation of truncated truncated versions (*At*GORK$^{623}$ and *At*GORK$^{510}$),
440 we followed similar procedures as above.

441

442

443 **Cryo-EM grid preparation and data acquisition**

444 The protein sample (4 µl, ~3.5 mg/ml) was applied to freshly glow-discharged holy
445 carbon film grids (Quantifoil, Cu, R1.2/1.3, 300 mesh) and blotted for 6.5 seconds at
446 100% humidity and 4°C using a Vitrobot Mark IV (Thermo Fisher Scientific), followed
447 by plunge freezing into liquid ethane.

448 All the films were collected on a Titan Krios transmission electron microscope
449 (Thermo Fisher Scientific, USA) operated at 300 kV equipped with a Gatan K2 or K3
450 Summit direct detection camera (Gatan Company, USA). Movies were recorded at
451 22,500× (for K3, corresponding 1.06 Å per pixel) or 130,000 × (for K2 summit,
452 corresponding 1.04 Å per pixel) nominal magnifications, using SerialEM software with
453 a beam-image shift method[40-41], at a total dose of 50 e-/Å2 distributed over 32 frames,
454 with defocus values between -1.2 and -2.2 µm.

455

456 **Data processing and model building**

457 All image processing steps were conducted using either CryoSPARC 3.1[42] or RELION
458 3.0[43]. CryoSPARC 3.1 was primarily used for reconstruction, while RELION 3.0 was
459 employed for alignment-free 3D classification to identify an alternate conformation
460 (*At*GORK$^{FL2}$) of the wild-type structure. Angular information was converted using
461 PyEM, and map analysis and adjustments were performed with UCSF Chimera[44].

462 Raw movie frames were aligned using a dose-weighted patch alignment method,
463 followed by CTF estimation. Particle picking was performed an oval template (88 ×
464 168 Å), and coordinates were screened using normalized cross-correlation and local
465 power scores to eliminate false positives. Particles were then down-sampled to a quarter
466 size and classified based on shape (circular for top-view projections and T-shaped for
467 side-view projections) after initial 2D classification to improve classification efficacy.
468 A preliminary 3D reconstruction was generated from a small subset of particles.

469 *At*GORK$^{FL1}$ was constructed with Nu-refinement using C2 symmetry with
470 156,313 particles, while *At*GORK$^{FL2}$ used 39,551 particles with C1 symmetry. The

471 resolutions were 3.4 Å for *At*GORK$^{FL1}$ and 4.3 Å for *At*GORK$^{FL2}$, respectively. The
472 alphafold2-predicted *Arabidopsis* GORK structure was used as the initial model, fitted
473 by individual domains in UCSF ChimeraX[45], and refined iteratively in Coot[46] and
474 PHENIX[47], and corrected iteratively. For the truncated *At*GORK$^{623}$ and *At*GORK$^{510}$,
475 the TMD structure from *At*GORK$^{FL1}$ was used as the initial model, followed by iterative
476 refinement and iterative adjustments in Coot and PHENIX. The resolutions were 3.2 Å
477 for *At*GORK$^{623}$ and 3.4 Å for *At*GORK$^{510}$, respectively. All figures were generated
478 using UCSF ChimeraX.
479
480 **Electrophysiology**
481 The electrophysiological experiments were performed as previously described[48].
482 Briefly, untagged coding sequences of *At*GORK wild type or mutated variants were
483 cloned into the pGHME2 vector for expression in *Xenopus* oocytes. cRNAs were
484 synthesized using T7 polymerase with linearized plasmid DNA templates. Oocyte sacs
485 were extracted and digested with 0.2 mg/ml collagenase (Sigma) in OR2 buffer (82.5
486 mM NaCl, 2.5 mM KCl, 1 mM $MgCl_2$, and 5 mM HEPES-Na pH 7.5). For expression,
487 36 ng of wild-type GORK cRNA was injected per oocyte, with mutant cRNA doses
488 adjusted to equimolar concentrations. Injected oocytes were incubated at 18°C in ND96
489 buffer (96 mM NaCl, 1.8 mM $CaCl_2$, 1 mM $MgCl_2$, 2 mM KCl, and 5 mM HEPES-Na
490 pH 7.5) for 48 hours before use.
491 TEVC recordings were performed using an OC-725C amplifier (Warner
492 Instruments) and Digidata 1550B (Molecular Devices) controlled by pClamp software.
493 The bath solution contained (in mM): 10 KCl, 90 NaCl, 1 $CaCl_2$, 2 $MgCl_2$, and 10
494 Tris/MES (pH 7.4), with osmolarity adjusted to ~220 mOsmol/kg using D-mannitol.
495 Microelectrodes (0.5-1 MΩ resistance) were filled with 3 M KCl, and agar bridges
496 served as bath electrodes. Voltage steps from -110 mV to +70 mV (20-mV increments,
497 2,000 ms duration) were applied, followed by -110 mV clamping for 450 ms, 4,000 ms,
498 or 16,000 ms depending on deactivation kinetics. Steady-state currents were measured

499 at 50 ms before the end of each step. Data were analyzed using Clampfit 10.6
500 (Molecular Devices), Prism 8.0 (GraphPad), and Origin 2021.
501
502 **Fluorescence and confocal imaging**
503 To assess the cell-surface expression of full-length and C-terminal truncated GORK
504 channels in *Xenopus* oocytes, GFP was fused to the N-terminus of each construct. The
505 corresponding cRNAs were injected into oocytes, which were then incubated at 18°C
506 for ~48 hours in ND96 buffer (detailed in the *Electrophysiology* section). GFP-tagged
507 protein expression was verified using a confocal laser scanning microscope (Zeiss LSM
508 980), and fluorescence intensities were quantified with ImageJ. To minimize variability
509 in expression levels due to experimental factors (e.g., cRNA injection dose or
510 incubation time), all experiments were performed in parallel.
511
512 **Data availability:**
513 All data generated or analysed in this paper are presented in the main text, figures and
514 the extended data figures and supplementary videos, or are available from the
515 corresponding author upon request. The cryo-EM maps of the *At*GORK full-length
516 (*At*GORK$^{FL1}$ and *At*GORK$^{FL2}$) and truncated version (*A*GORK$^{623}$ and *A*GORK$^{510}$) have
517 been deposited in the Electron Microscopy Data Bank with accession codes EMD-
518 62338, EMD-37500, EMD-62337 and EMD-62339, respectively, and their structural
519 models have been deposited in the PDB with accession codes 9KHF, 8WFZ, 9KHE and
520 9KHG, respectively (Table S1, Supporting Information).
521
522 **Acknowledgments:**
523 This project is financially supported by the National Key Research and Development
524 Program of China (2020YFA0509903, 2016YFA0500503 and 2021YFA1300702), the
525 National Natural Science Foundation of China (32300257, 31322005 and 31470728),

and The Chinese Academy of Sciences Project for Young Scientists in Basic Research (YSRB-119).

**Author contributions:** Q.-Y.L. performed protein purification, Cryo-EM data collection, data analysis and mutant design; L.-H.T. and C.-R.Z performed Cryo-EM data collection, structural determination and analysis; L.Q. performed electrophysiology and data analysis, K.-W. and G.-H.Z. performed experiments; S.-G.H., Q.X., T.-X.N. and M.S. analyzed data; R.H., analyzed data and wrote the manuscript, Y.-H.C. initiated the project, planned and analyzed experiments, supervised the research, and wrote the manuscript with input from all authors.

**Competing interests:** The authors declare no competing interests.

## Reference

[1] F. J. Maathuis, *Curr. Opin. Plant Biol.* **2009**, *12*, 250.
[2] T. Sharma, I. Dreyer, J. Riedelsberger, *Front Plant Sci.* **2013**, *4*, 224.
[3] R. Hedrich, *Physiol. Rev.* **2012**, *92*, 1777.
[4] P. Mäser, S. b. Thomine, J. I. Schroeder, J. M. Ward, K. Hirschi, H. Sze, I. N. Talke, A. Amtmann, F. J. M. Maathuis, D. Sanders, J. F. Harper, J. Tchieu, M. Gribskov, M. W. Persans, D. E. Salt, S. A. Kim, M. L. Guerinot, *Plant Physiol.* **2001**, *126*, 1646.
[5] A. A. Very, H. Sentenac, *Annu. Rev. Plant Biol.* **2003**, *54*, 575.
[6] A. Amtmann, P. Armengaud, V. Volkov, in **2004**.
[7] Y. Wang, W. H. Wu, *Mol Plant.* **2010**, *3*, 280.
[8] P. Ache, D. Becker, N. Ivashikina, P. Dietrich, M. R. G. Roelfsema, R. Hedrich, *FEBS Lett.* **2000**, *486*, 93.
[9] T. H. Kim, M. Böhmer, H. Hu, N. Nishimura, J. I. Schroeder, *Annu. Rev. Plant Biol.* **2010**, *61*, 561.
[10] S. Förster, L. K. Schmidt, E. Kopic, U. Anschütz, S. Huang, K. Schlücking, P. Köster, R. Waadt, A. Larrieu, O. Batistič, P. L. Rodriguez, E. Grill, J. Kudla, D. Becker, *Dev. Cell.* **2019**, *48*, 87.
[11] Y. Xie, Y. Mao, W. Zhang, D. Lai, Q. Wang, W. Shen, *Plant Physiol.* **2014**, *165*, 759.
[12] E. Hosy, A. Vavasseur, K. Mouline, I. Dreyer, F. Gaymard, F. Porée, J. Boucherez, A. Lebaudy, D. Bouchez, A.-A. Véry, T. Simonneau, J.-B. Thibaud, H. Sentenac, *Proc. Natl. Acad. Sci. USA.* **2003**, *100*, 5549.
[13] J. I. Schroeder, *Proc Natl Acad Sci U S A.* **2003**, *100*, 4976.
[14] A. M. Hetherington, F. I. Woodward, *Nature.* **2003**, *424*, 901.

[15] T. Lawson, S. Vialet-Chabrand, *New Phytol.* **2019**, *221*, 93.
[16] F. C. Sussmilch, M. R. G. Roelfsema, R. Hedrich, *New Phytol.* **2019**, *222*, 84.
[17] Y. Murata, I. C. Mori, S. Munemasa, *Annu. Rev. Plant Biol.* **2015**, *66*, 369.
[18] A. M. Hetherington, *Cell.* **2001**, *107*, 711.
[19] R. Hedrich, D. Geiger, *New Phytol.* **2017**, *216*, 46.
[20] M. D. Clark, G. F. Contreras, R. Shen, E. Perozo, *Nature.* **2020**, *583*, 145.
[21] S. Y. Li, F. Yang, D. M. Sun, Y. Zhang, M. G. Zhang, S. L. Liu, P. Zhou, C. W. Shi, L. H. Zhang, C. L. Tian, *Cell Res.* **2020**, *30*, 1049.
[22] S. B. Long, E. B. Campbell, R. Mackinnon, *Science.* **2005**, *309*, 903.
[23] J. Payandeh, T. Scheuer, N. Zheng, W. A. Catterall, *Nature.* **2011**, *475*, 353.
[24] Y. Zhou, J. H. Morais-Cabral, A. Kaufman, R. Mackinnon, *Nature.* **2001**, *414*, 43.
[25] C. H. Lee, R. MacKinnon, *Cell.* **2017**, *168*, 111.
[26] S. Li, Y. Wang, C. Wang, Y. Zhang, D. Sun, P. Zhou, C. Tian, S. Liu, *Cell Discov.* **2023**, *9*, 67.
[27] Y. M. Lu, M. Yu, Y. T. Jia, F. Yang, Y. M. Zhang, X. Xu, X. M. Li, F. Yang, J. L. Lei, Y. Wang, G. H. Yang, *Nat Commun.* **2022**, *13*.
[28] O. S. Smart, J. G. Neduvelil, X. Wang, B. A. Wallace, M. S. Sansom, *J Mol Graph.* **1996**, *14*, 354.
[29] G. E. Flynn, K. D. Black, L. D. Islas, B. Sankaran, W. N. Zagotta, *Structure.* **2007**, *15*, 671.
[30] J. Xue, Y. Han, W. Zeng, Y. Wang, Y. Jiang, *Neuron.* **2021**, *109*, 1302.
[31] M. S. Dickinson, S. Pourmal, M. Gupta, M. Bi, R. M. Stroud, *Biochem.* **2022**, *61*, 2177.
[32] D. H. Kwon, F. Zhang, B. A. McCray, S. Feng, M. Kumar, J. M. Sullivan, W. Im, C. J. Sumner, S. Y. Lee, *Nat Commun.* **2023**, *14*, 3732.
[33] X. Zhang, W. Carroll, T. B. Nguyen, T. H. Nguyen, Z. Yang, M. Ma, X. Huang, A. Hills, H. Guo, R. Karnik, M. R. Blatt, P. Zhang, *Nat Commun.* **2025**, *16*, 1961.
[34] S. G. Sedgwick, S. J. Smerdon, *Trends Biochem. Sci.* **1999**, *24*, 311.
[35] J. Li, A. Mahajan, M.-D. Tsai, *Biochemistry.* **2006**, *45*, 15168.
[36] P. J. M. van Kleeff, J. Gao, S. Mol, N. Zwart, H. Zhang, K. W. Li, A. H. de Boer, *Plant Physiol. Biochem.* **2018**, *125*, 219.
[37] C. Corratgé-Faillie, E. Ronzier, F. Sanchez, K. Prado, J.-H. Kim, S. Lanciano, N. Leonhardt, B. Lacombe, T. C. Xiong, *FEBS Lett.* **2017**, *591*, 1982.
[38] C. Lefoulon, M. Boeglin, B. Moreau, A. A. Very, W. Szponarski, M. Dauzat, E. Michard, I. Gaillard, I. Cherel, *J. Biol. Chem.* **2016**, *291*, 6521.
[39] L. Qin, Y. N. Deng, X. Y. Zhang, L. H. Tang, C. R. Zhang, S. M. Xu, K. Wang, M. H. Wang, X. H. Zhang, M. Su, Q. Xie, W. A. Hendrickson, Y. H. Chen, *Proc Natl Acad Sci U S A.* **2024**, *121*, e2323040121.
[40] C. Wu, X. Huang, J. Cheng, D. Zhu, X. Zhang, *J Struct Biol.* **2019**, *208*, 107396.
[41] D. N. Mastronarde, *J Struct Biol.* **2005**, *152*, 36.
[42] A. Punjani, J. L. Rubinstein, D. J. Fleet, M. A. Brubaker, *Nat. Methods.* **2017**, *14*, 290.
[43] J. Zivanov, T. Nakane, B. O. Forsberg, D. Kimanius, W. J. Hagen, E. Lindahl, S. H. Scheres, *Elife.* **2018**, *7*.
[44] E. F. Pettersen, T. D. Goddard, C. C. Huang, G. S. Couch, D. M. Greenblatt, E. C. Meng, T. E. Ferrin, *J Comput Chem.* **2004**, *25*, 1605.

[45] E. F. Pettersen, T. D. Goddard, C. C. Huang, E. C. Meng, G. S. Couch, T. I. Croll, J. H. Morris, T. E. Ferrin, *Protein Sci.* **2021**, *30*, 70.

[46] P. Emsley, B. Lohkamp, W. G. Scott, K. Cowtan, *Acta Crystallogr D Biol Crystallogr.* **2010**, *66*, 486.

[47] D. Liebschner, P. V. Afonine, M. L. Baker, G. Bunkóczi, V. B. Chen, T. I. Croll, B. Hintze, L. W. Hung, S. Jain, A. J. McCoy, N. W. Moriarty, R. D. Oeffner, B. K. Poon, M. G. Prisant, R. J. Read, J. S. Richardson, D. C. Richardson, M. D. Sammito, O. V. Sobolev, D. H. Stockwell, T. C. Terwilliger, A. G. Urzhumtsev, L. L. Videau, C. J. Williams, P. D. Adams, *Acta Crystallogr D Struct Biol.* **2019**, *75*, 861.

[48] Y. N. Deng, H. Kashtoh, Q. Wang, G. X. Zhen, Q. Y. Li, L. H. Tang, H. L. Gao, C. R. Zhang, L. Qin, M. Su, F. Li, X. H. Huang, Y. C. Wang, Q. Xie, O. B. Clarke, W. A. Hendrickson, Y. H. Chen, *Proc Natl Acad Sci U S A.* **2021**, *118*.

616 **Figure legends**

617 **Figure 1. Architecture of the Arabidopsis GORK**

618 A) Schematic diagram of the domain architecture in Arabidopsis GORK (*At*GORK).
619 The transmembrane domain (TMD, blue), the C-linker domain (C-linker, Cyan), the
620 cyclic nucleotide-binding domain homolog (CNBDH, purple) and the Ankyrin domain
621 (ANK, orange) are shown. B, C) The cartoon drawing of the *At*GORK tetramer. One
622 protomer is colored as indicated in (A), and other protomers are colored in grey. D)
623 Symmetry reduction (from C4 to C2) within the tetrameric assembly. This represents a
624 unique structural feature of the GORK family and likely serves as a unique mechanism
625 for channel regulation. The current *At*GORK structure likely represents an
626 autoinhibited, pre-activation state. Different protomers are indicated with letter A-D. E)
627 Structural superimposition of protomer A with its neighboring protomer B.

628

629 **Figure 2. Structural domains of *At*GORK: TMD, C-linker, CNBDH and ANK.**

630 A) Ribbons drawing of the TMD/C-linker portion, with two protomers (A and C) are
631 shown, colored and oriented as in Figure 1C. The VSD is connected to the PD through
632 a short linker, resulting in a "non-domain-swapped" configuration. The pore-lining
633 surface was computed by the program HOLE and drawn into a cartoon model of the
634 GORK channel pore in a closed conformation. Critical residue in VSD (R174, R177,
635 R179, and R187), selectivity filter ($^{271}$TVGYG$^{275}$) and the narrowest constrictions (I303
636 and T307) are shown in sticks. The S4 helix adopt a resting "up" conformation, similar
637 to that in plant inward-rectifying KAT1 and AKT1. B) Structural comparison of the C-
638 linker of protomer A ("kinked" conformation) with protomer B ("flat" conformation).
639 The "flat" conformation of the C-linker actually disrupts the formation of a C4
640 symmetrical gating ring, resulting in decoupling between the transmembrane helices
641 with the cytoplasmic domains, ultimately affecting channel gating. C) Ribbons drawing
642 of the C-linker/CNBDH portion. D) Ribbons drawing of the dimeric ANK portion.
643 ANKs from two neighboring protomers tightly interact, creating a buried area of ~1500

644 Å$^2$. The first three and the last three repeats are tandem units. Repeats 1-2/4-5 are
645 canonical α-helix/α-helix/β-hairpin motifs, while repeat 3/6 lacks the β-hairpin. The
646 presence of the ANK domain and its dimerization are unique features of the GORK
647 family. ANK dimerization leads to symmetry reduction in the tetrameric channel. This,
648 in turn, affects the coupling between the transmembrane helices and cytoplasmic
649 domains, ultimately holding the ion channel in an autoinhibited, pre-activation state.
650
651 **Figure 3. ANK plays an inhibitory role in regulating *At*GORK.**
652 A) Ribbons drawing of the ANK dimeric domain, with truncated points or mutated
653 loops are highlighted with red arrows or in red boxes. B, C) The C-terminal truncation
654 of *At*GORK, with representative current traces in (B) and steady-state current-voltage
655 (*I-V*) relations in (C). Truncating half ANK domain (Δ624-820, residues 1-623) or the
656 entire ANK domain (Δ544-820, residues 1-543) significantly increased currents.
657 However, a further truncation (Δ511-820, residues 1-510) disrupted the channel activity.
658 D, E) The loop-substitution in ANK of *At*GORK, with representative current traces in
659 (D) and steady-state current-voltage (*I-V*) relations in (E). Substitution of loops between
660 repeats 1/2 and 2/3 with "SGGG" significantly enhanced GORK activity. However,
661 similar replacement of the loops between repeats 4/5 and 5/6 impaired GORK function.
662 Data are mean ± SEM, n ≥ 8.
663
664 **Figure 4. Mutational tests on conserved acidic residues at the C-linker/TMD**
665 **interface.**
666 A) Ribbons drawing of the C-linkers in tetrameric assembly, highlighting negatively
667 charged residues (E317, D321, D325) in sticks. B) Close-up view of the interface
668 between the C-linker and TMD. E317 and D321 (C-linker of protomer A) form ionic
669 interactions with K312 (Helix S6' of protomer D), while R200 (Helix S5 of protomer
670 A) forms a salt bridge with E317 from its adjacent protomer B. C-G)
671 Electrophysiological analyses of E317, D321 and D325 mutations in *At*GORK$^{543}$.

672 Representative current traces (C) and steady-state current-voltage (*I-V*) relations (D)
673 are shown. Relative conductance-voltage ($G_{relative}$-$V$) curves (E) and half-activation
674 voltage ($V_{1/2}$) values (F) were generated through Boltzmann sigmoidal fitting (outliers
675 excluded). Conductance was calculated using the equation $G = I/(V - E_K)$, where $I$ is the
676 steady-state current, $V$ is the test potential, and $E_K$ (–58 mV) was derived from the
677 Nernst equation based on intracellular (~100 mM) and extracellular (10 mM) $K^+$
678 concentration in the oocyte TEVC recordings. Relative conductance was calculated by
679 normalization to the maximal conductance. Half-time ($t_{1/2}$) for activation at +70 mV
680 and deactivation at −110 mV, calculated as ln (2)·τ where τ is the time constant from
681 single-exponential decay fitting, is shown in (G). Data are mean ± SEM, n ≥ 8.
682 Significance analysis was performed using unpaired Student's t-test, with P-values
683 displayed on the bar charts.
684
685 **Figure 5. Structural comparison of the auto-inhibited *At*GORK and the ANK-**
686 **truncated variants.**
687 A) Superimposition of the ANK-truncated variants (*At*GORK$^{623}$ and *At*GORK$^{510}$), with
688 each protomer of *At*GORK$^{623}$ shown in different color, while all four protomers in
689 *At*GORK$^{510}$ are displayed in grey. Both truncated mutants showed nearly identical
690 structures, with a root-mean-square deviation (RMSD) of approximately 0.48 Å for
691 their superimposed tetramers. B-D) Close-up views of S4-S5 helix regions in the
692 superimposed protomers of *At*GORK$^{FL1}$ and *At*GORK$^{623}$. (B) compares protomer A
693 (blue) and protomer B (grey) of *At*GORK$^{FL1}$, while (C) shows all four protomers of
694 *At*GORK$^{623}$. These comparisons reveal that *At*GORK$^{FL1}$ exhibits quasi-C4 symmetry,
695 whereas *At*GORK$^{623}$ has strict C4 symmetry. The displacement of Cα position of
696 Tyr196 in the C4-C5 region is approximately 3.8 Å (indicated by yellow dash-line). (D)
697 further compares protomers A and B of both *At*GORK$^{FL1}$ and *At*GORK$^{623}$, showing that
698 the protomers in *At*GORK$^{623}$ closely resembles protomer A in *At*GORK$^{FL1}$, rather than

699 protomer B. ANK truncation in *At*GORK$^{623}$ restores C4 symmetry in the tetrameric
700 assemblies.
701
702 **Figure 6. A model of symmetry conversion in plant GORK regulation.**
703 The GORK structure in the autoinhibited state (left, Cryo-EM) exhibits C2 symmetry,
704 while in the activatable state (right, Alphafold3 prediction), it exhibits C4 symmetry.
705 In brief, ANK dimerization reduces the symmetry of the GORK tetramer from C4 to
706 C2, resulting in an autoinhibited state. Disrupting dimerization restores C4 symmetry,
707 converting GORK to an activatable state. This dynamic symmetry conversion in the
708 GORK tetramer provides a unique mechanism for regulating channel activity, enabling
709 transitions between inhibited and activatable states - a distinctive feature of GORK
710 family proteins containing the ANK domain. In such a way, ANK functions as a
711 molecular switch, regulating the GORK channel in guard cells and controlling stomatal
712 movement in response to environmental stimuli.
713
714
715

# Figure 1

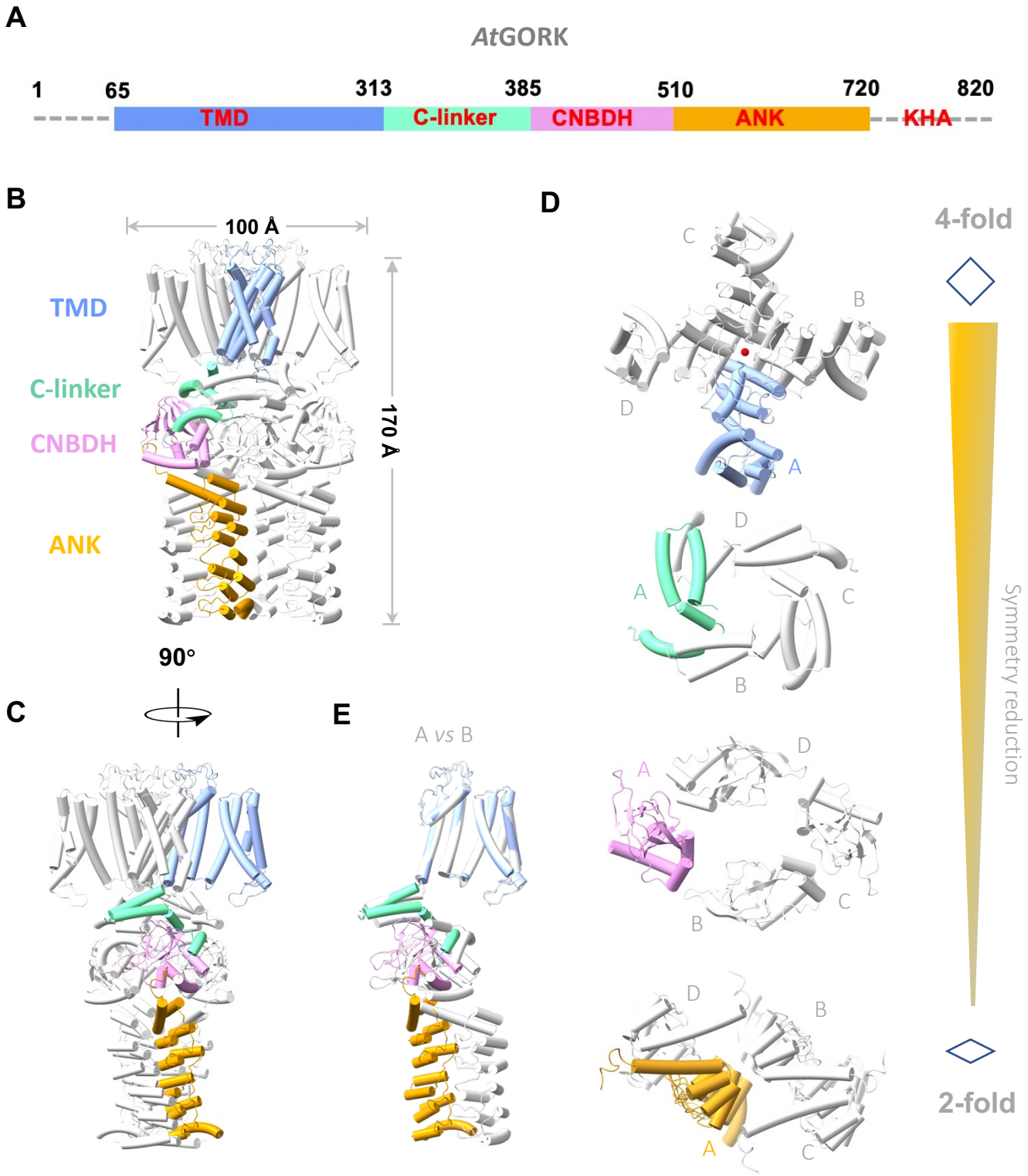
A
AtGORK
1
65
313
385
510
720
820
TMD
C-linker
CNBDH
ANK
KHA
B
100 Å
TMD
C-linker
CNBDH
ANK
170 Å
90°
C
E
A vs B
D
4-fold
C
B
D
A
D
A
C
B
A
D
B
C
D
B
A
C
Symmetry reduction
2-fold

# Figure 2

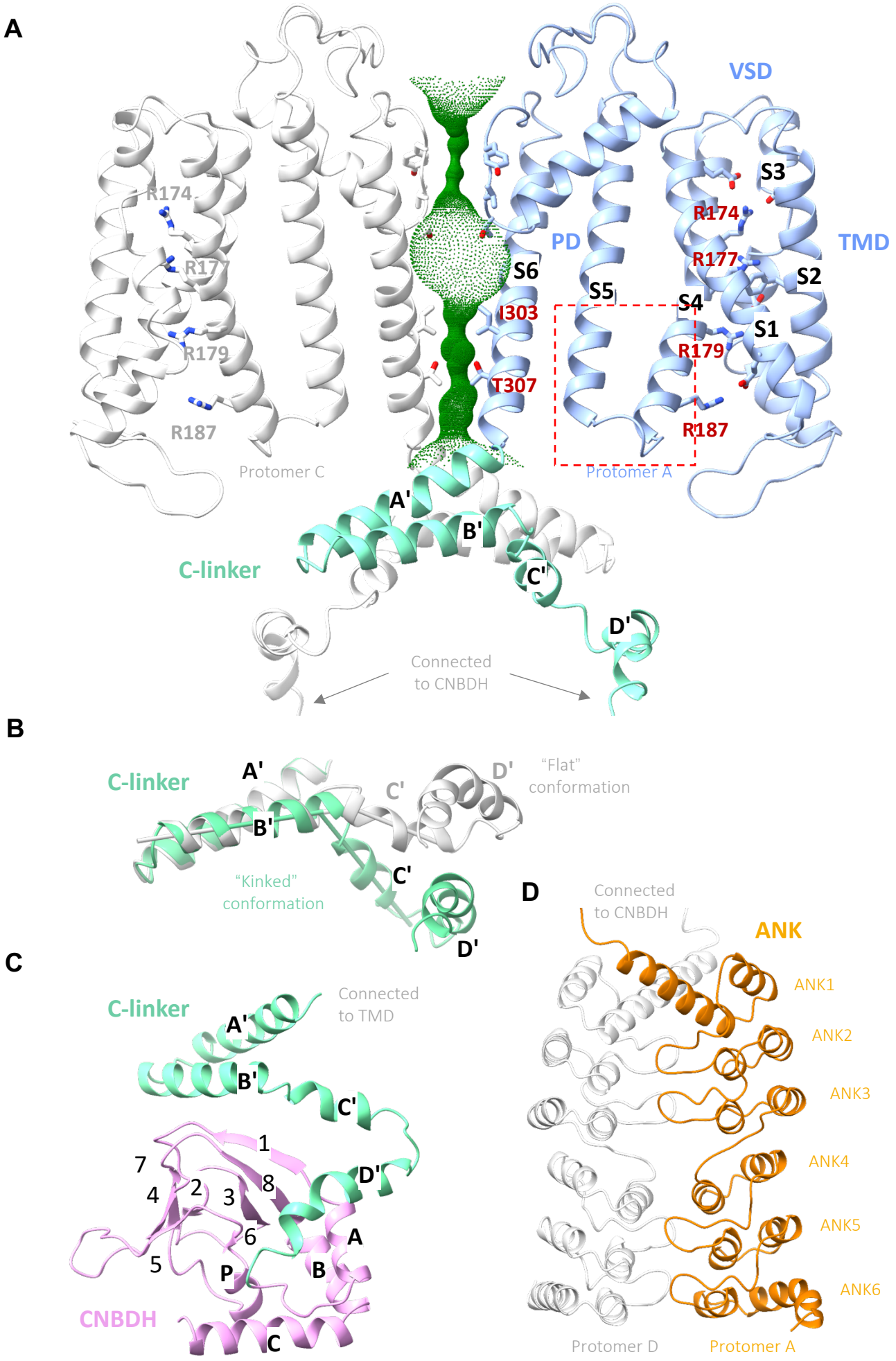
A
VSD
S3
R174
PD
TMD
R177
S6
S2
S5
S4
I303
S1
R179
T307
R187
R174
R177
R179
R187
Protomer C
Protomer A
A'
B'
C-linker
C'
D'
Connected
to CNBDH
B
C-linker
A'
C'
D'
"Flat"
conformation
B'
"Kinked"
conformation
C'
D'
C
C-linker
Connected
to TMD
A'
B'
C'
1
7
D'
4
2
3
8
6
A
5
P
B
CNBDH
C
D
Connected
to CNBDH
ANK
ANK1
ANK2
ANK3
ANK4
ANK5
ANK6
Protomer D
Protomer A

# Figure 3

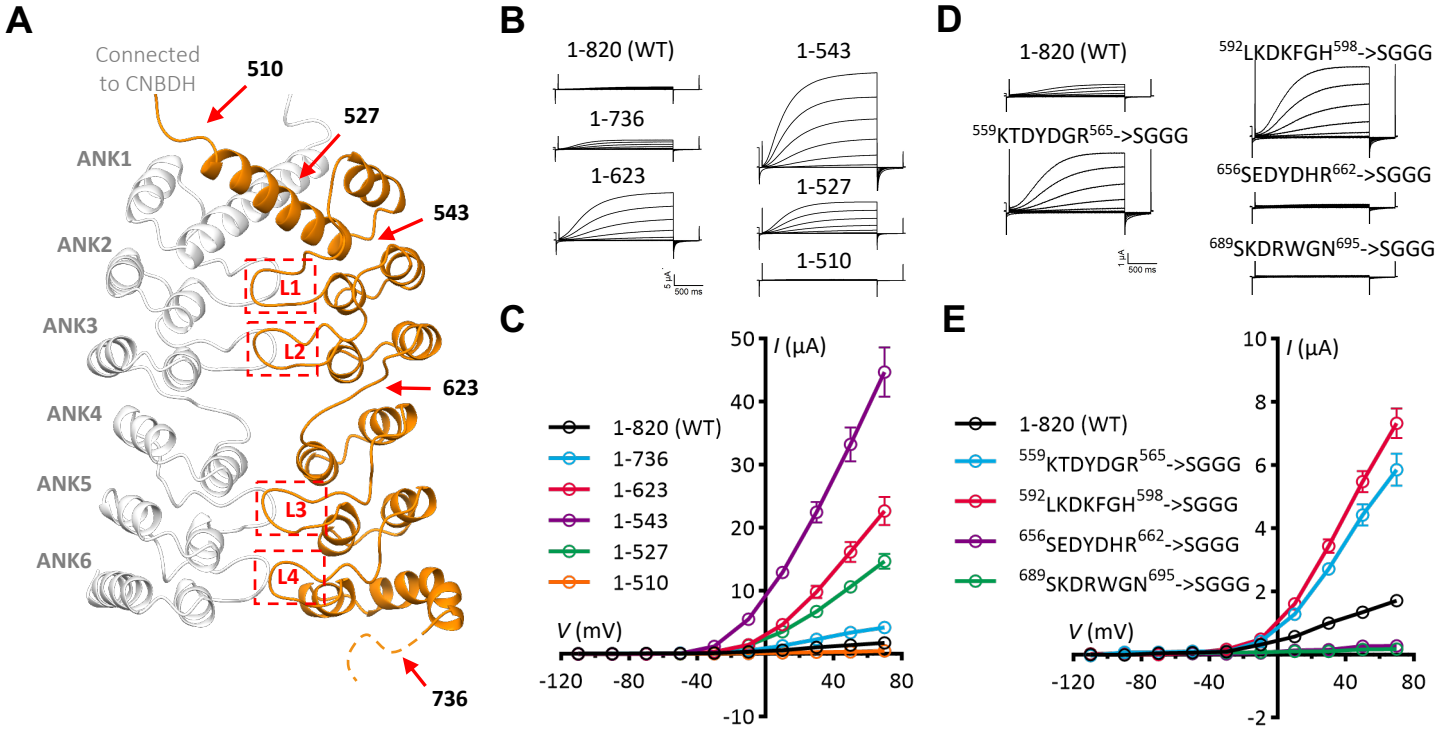
A
Connected to CNBDH
510
527
543
623
736
ANK1
ANK2
ANK3
ANK4
ANK5
ANK6
L1
L2
L3
L4
B
1-820 (WT)
1-736
1-623
1-543
1-527
1-510
C
I (µA)
V (mV)
1-820 (WT)
1-736
1-623
1-543
1-527
1-510
D
1-820 (WT)
559KTDYDGR565->SGGG
592LKDKFGH598->SGGG
656SEDYDHR662->SGGG
689SKDRWGN695->SGGG
E
I (µA)
V (mV)
1-820 (WT)
559KTDYDGR565->SGGG
592LKDKFGH598->SGGG
656SEDYDHR662->SGGG
689SKDRWGN695->SGGG

# Figure 4

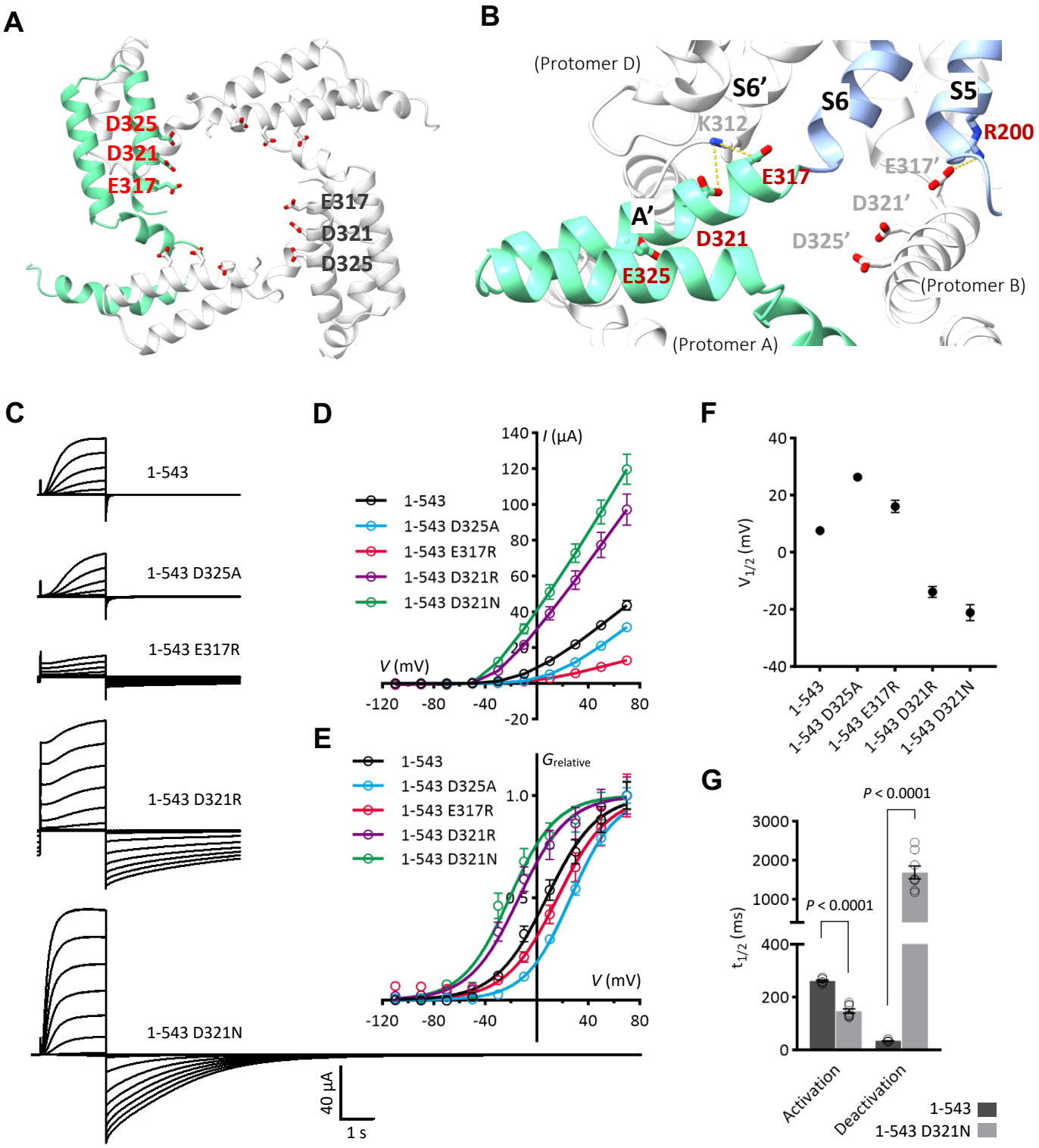
A
D325
D321
E317
E317
D321
D325
B
(Protomer D)
S6'
S6
S5
K312
R200
E317
E317'
D321'
A'
D321
D325'
E325
(Protomer B)
(Protomer A)
C
1-543
1-543 D325A
1-543 E317R
1-543 D321R
1-543 D321N
40 µA
1 s
D
I (µA)
1-543
1-543 D325A
1-543 E317R
1-543 D321R
1-543 D321N
V (mV)
E
Grelative
1-543
1-543 D325A
1-543 E317R
1-543 D321R
1-543 D321N
V (mV)
F
V1/2 (mV)
1-543
1-543 D325A
1-543 E317R
1-543 D321R
1-543 D321N
G
P < 0.0001
P < 0.0001
t1/2 (ms)
Activation
Deactivation
1-543
1-543 D321N

# Figure 5

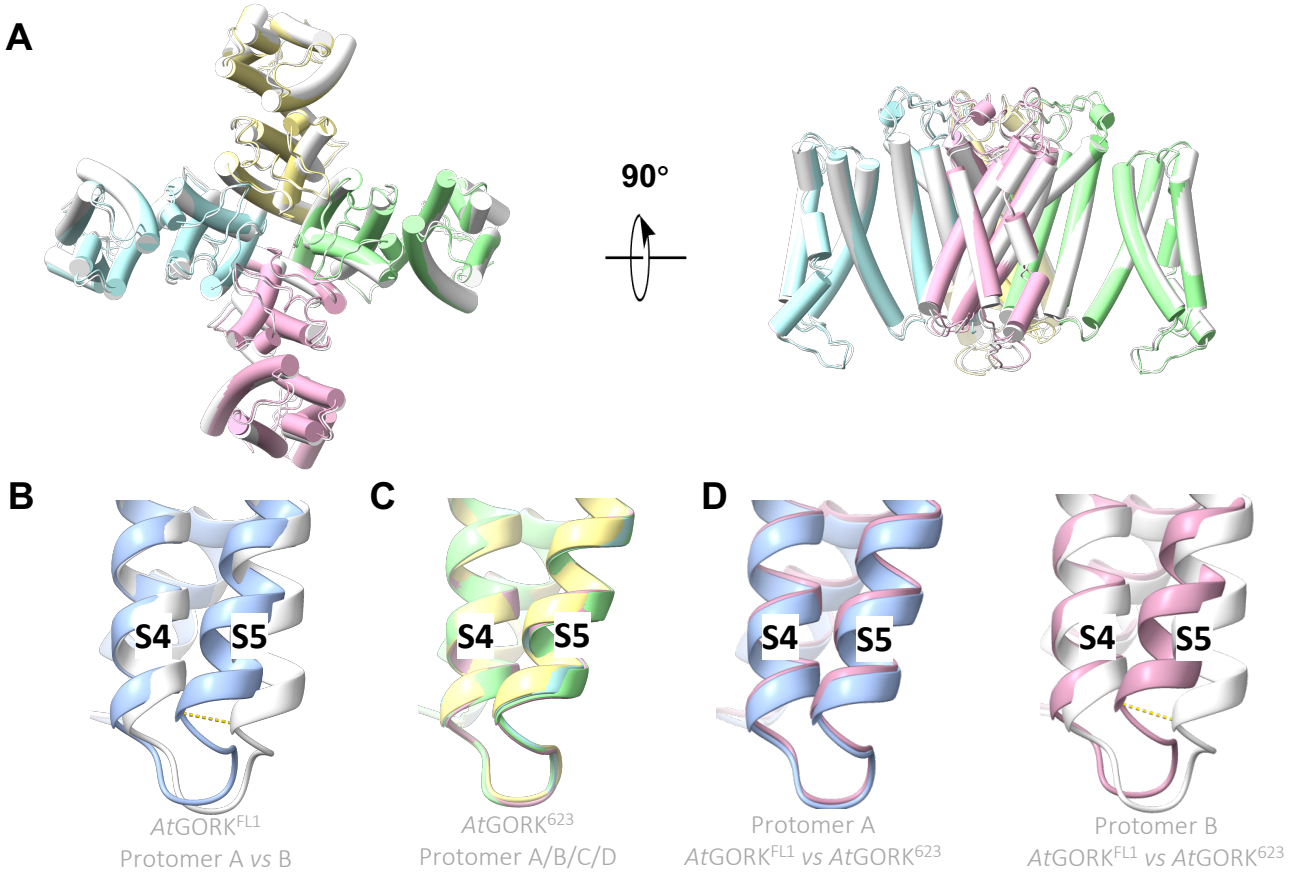
A
90°
B
S4
S5
AtGORK^FL1
Protomer A vs B
C
S4
S5
AtGORK^623
Protomer A/B/C/D
D
S4
S5
Protomer A
AtGORK^FL1 vs AtGORK^623
S4
S5
Protomer B
AtGORK^FL1 vs AtGORK^623

# Figure 6

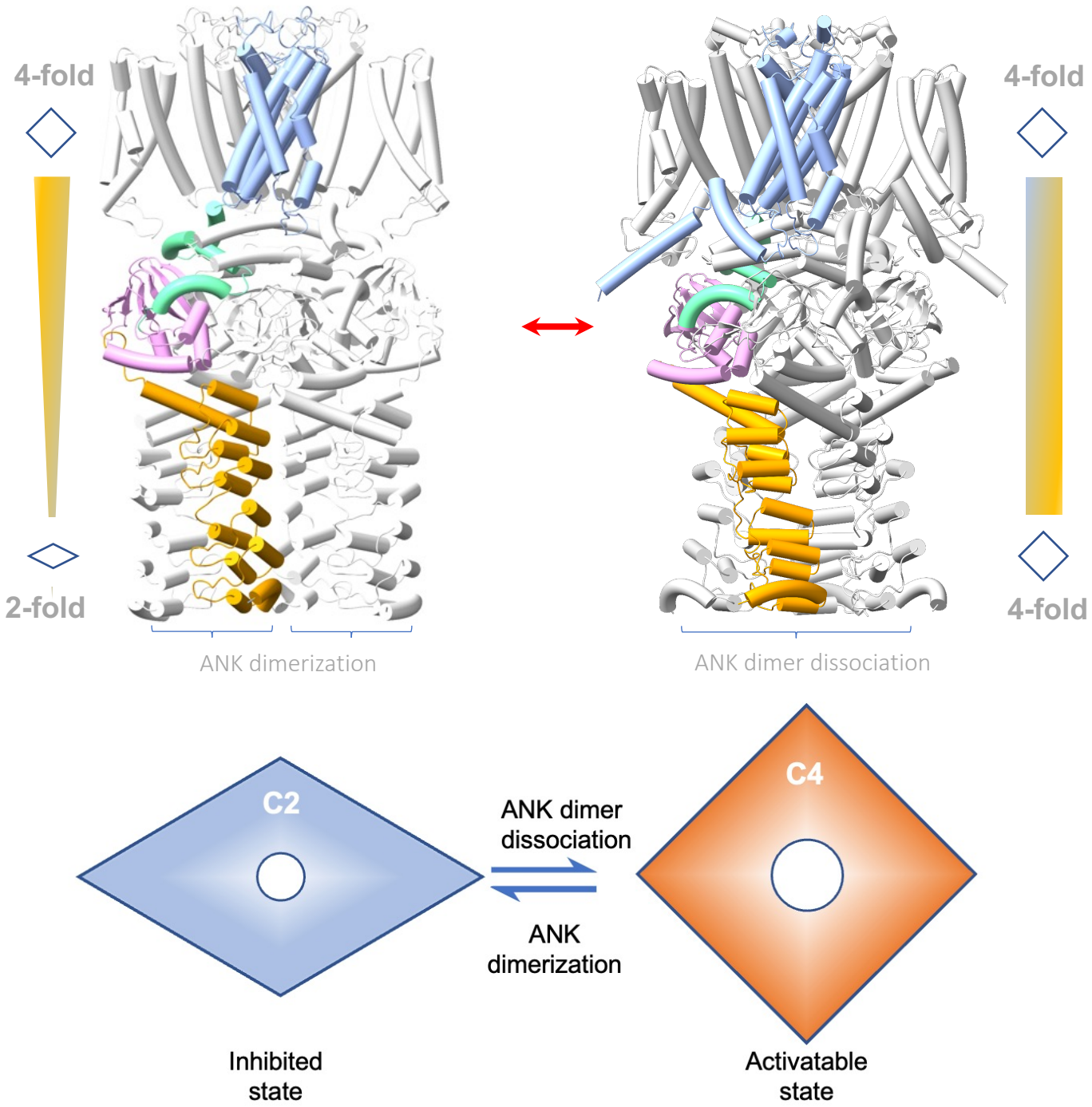
4-fold
2-fold
ANK dimerization
4-fold
4-fold
ANK dimer dissociation
C2
ANK dimer dissociation
ANK dimerization
C4
Inhibited state
Activatable state